npj | Materials Degradation

www.nature.com/npjmatdeg

ARTICLE OPEN

The fate of Si and Fe while nuclear glass alters with steel and clay

C. Carriere[1]✉, P. Dillmann[1], S. Gin[2], D. Neff[1], L. Gentaz[1], F. Bruguier[2], I. Monnet[3], E. Gardes[3], M. Saheb[4], E. Foy[1], N. Nuns[5], A. Delanoë[1], J. J. Dynes[6], N. Michau[7] and C. Martin[7]

The French concept developed to dispose high-level radioactive waste in geological repository relies on glassy waste forms, isolated from the claystone host rock by steel containers. Understanding interactions between glass and surrounding materials is key for assessing the performance of a such system. Here, isotopically tagged SON68 glass, steel and claystone were studied through an integrated mockup conducted at 50 °C for 2.5 years. Post-mortem analyses were performed from nanometric to millimetric scales using TEM, STXM, ToF-SIMS and SEM techniques. The glass alteration layer consisted of a crystallized Fe-rich smectite mineral, close to nontronite, supporting a dissolution/reprecipitation controlling mechanism for glass alteration. The mean glass dissolution rate ranged between 1.6×10^{-2} g m^{-2} d^{-1} to 3.0×10^{-2} g m^{-2} d^{-1}, a value only 3–5 times lower than the initial dissolution rate. Thermodynamic calculations highlighted a competition between nontronite and protective gel, explaining why in the present conditions the formation of a protective layer is prevented.

npj Materials Degradation (2021)5:16 ; https://doi.org/10.1038/s41529-021-00160-x

INTRODUCTION

In France, like in the other countries using nuclear power plants, plans for disposing high-level radioactive waste (HLW) in a deep geological repository are being developed. The selected rock is the Callovo–Oxfordian claystone (Cox) located in the North-East of the Parisian basin and the concept under consideration is based on the vitrified HLW poured in a stainless-steel canister and placed in a carbon steel overpack. The resulting waste package should be placed in horizontal tunnels dug into the low permeability claystone. However it is expected that groundwater will corrode the metallic envelopes and eventually reach the glass. This system essentially aims at delaying water arrival during the first period of the disposal[1]. From the safety standpoint the performance of each component must be evaluated, as well as that of the global system. Owing to the amount of radioactive elements that would be disposed of (roughly 20000 metric tons of glass with ~18 wt% waste loading made of fission products and minor actinides), such a disposal must be safe for a period of ~1 My. Performance assessment primarily relies on the calculation of the waste form durability and the migration of radionuclides in the geosphere. The release of radionuclides from the waste form depends on physicochemical parameters (chemical interactions, diffusion transport) and interactions between materials (glass/steel/clay) in contact with water[2,3]. The expected scenario would then be resaturation of clay, corrosion of the canisters, glass leaching and the release of radioelements[4]. Their dispersion/migration in the geosphere depends on many parameters such as clay sorption capacity, formation of secondary phases, microbial activity…[5]

Nuclear glass alteration has been studied for decades. SON68 glass, the inactive surrogate of R7T7 glass produced at La Hague is certainly one of the most studied borosilicate glass to date[6]. Several dissolution mechanisms were observed when glass is placed in contact with water[7]. The first step concerns coupled mechanisms, i.e., glass hydration, where water molecules penetrate the borosilicate network[8], and interdiffusion which exchanges protons contained in solution with alkali elements (i.e., Na, Li, Cs) in the glass. In parallel, hydrolysis of covalent bonds forming the glass network linkages (mostly Si-O-X (X = Si, Al, Zr, B) induces depolymerization of the silicate network. This reaction takes place at the hydrated layer/solution interface and releases of orthosilicic acid (H_4SiO_4) into solution. Sparingly soluble elements can either condense or precipitate at the glass surface, leading to the formation of a glass alteration layer (GAL), generally composed of Si, Al, Zr, Ca, and highly depleted in Na and B. Hydrolysis is characterized by the highest alteration rate, named initial dissolution rate (r_0), which can decrease by several orders of magnitude when an amorphous protective gel is formed at the glass/solution interface. The gel is formed either by in situ condensation of hydrolyzed Si within the gel[9], or by precipitation of aqueous species, depending on the glass composition and the alteration conditions[10–15]. The gel self-reorganizes and densifies[16]. Glass alteration is generally considered as isovolumetric, i.e., the gel replaces the glass maintaining the same volume of solids[17,18]. When the gel porosity is partly clogged at the gel/solution interface[19,20], it acts as a diffusion barrier that limits exchanges and slows down the global glass dissolution rate. Gels formed in circum-neutral pH conditions are stable in solution containing 50–100 ppm of dissolved Si[21–27], meaning that Si from the gel does not exchange with that from the solution in such conditions. In addition to the gel, secondary phases can precipitate (phyllosilicate, calcium-silicate-hydrates, zeolites) and impact both the gel properties and the solution chemistry[20,28,29]. In this case, the dissolved constituents of the glass, especially the Si, undergo both in situ condensation and precipitation[30].

[1]LAPA-IRAMAT, NIMBE, CEA, CNRS, Université Paris-Saclay, CEA Saclay, Gif-sur-Yvette, France. [2]CEA, DES, ISEC, DE2D, Université de Montpellier, Marcoule, Bagnols sur Cèze, France. [3]Centre de Recherche sur les Matériaux, les Ions et la Photonique (CIMAP), CEA-CNRS-ENSICAEN, Caen cedex 5, France. [4]Laboratoire Interuniversitaire des Systèmes Atmosphériques, LISA, UMR CNRS 7583, Université Paris Est Créteil et Université Paris Diderot, Institut Pierre Simon Laplace, Créteil Cedex, France. [5]Université Lille1 Sciences et Technologies, Institut des Molécules et de la Matière Condensée de Lille, Villeneuve d'Ascq cedex, France. [6]Canadian Light Source, Saskatoon, SK, Canada. [7]Andra, Direction Recherche et Développement, Châtenay-Malabry, France. ✉email: charly.carriere@cea.fr

Published in partnership with CSCP and USTB

npj nature partner journals

Whatever the mechanism at play, i.e., hydrolysis/condensation or dissolution/reprecipitation, the fate of Si during glass alteration is crucial as it controls the glass behavior[31]. A few studies have focused on glass alteration mechanisms following Si migration in isotopic ^{29}Si leaching experiments and secondary ion mass spectrometry (SIMS) $^{29}Si/^{28}Si$ ratio detection[30,32,33]. They observed that the gel had a $^{29}Si/^{28}Si$ ratio intermediate between glass and solution, and an outer phyllosilicate-rich layer with a $^{29}Si/^{28}Si$ ratio close to the one detected in solution, clear evidence that the hydrolysis/condensation or dissolution/reprecipitation can take place simultaneously. A recent study demonstrated that the two mechanisms can control sequentially glass corrosion[10].

The above-mentioned studies were conducted in the absence of iron. Iron ions as a result of steel corrosion can precipitate with Si to form Fe-Si-O phases. These phases are assimilated to phyllosilicates and could impact the glass alteration mechanisms and kinetics[26,34–39]. As an example, Neill et al.[26] altered ISG glass at 90 °C and pH 7 in a ^{29}Si saturated solution and after 70 days—a duration allowing the formation of a dense and protective gel layer—magnetite (Fe_3O_4) was added leading to a drop in the ^{29}Si concentration, followed by a subsequent resumption of alteration. Although global trends were observed, current models such as GM2001 or GRAAL[2,40,41], cannot predict quantitatively the glass behavior in such complex environments. For that reason, a better experimental understanding of the interactions between glass, steel and clay is necessary.

Here, we studied the influence of iron and claystone on glass alteration mechanisms and kinetics. We focused on a SON68 nuclear glass/steel/claystone system, as presented in Fig. 1. A piece of SON68 glass doped with ^{57}Fe and ^{29}Si, with one face in near-contact with a piece of iron was altered for 2.5 years at 50 °C in a core of water saturated Cox claystone (Fig. 1). Post-mortem characterization techniques were used to identify the alteration products and assess the fate of Si. We demonstrate that Fe from the iron piece reacted with Si from the glass to form nontronite, leading to a high glass dissolution rate and a low dispersion of Si released by the glass.

RESULTS

Glass/steel interface

A large area view of the glass/iron/claystone system using Scanning Electron Microscopy (SEM), focusing on the reaction products at the doped glass/metallic iron interface, with the metallic iron on the top and the doped pristine glass (PG) on the bottom is shown in Fig. 2a. On the right-hand side (where the iron corrosion products (ICP) are thickest), a layer is present in the embedding resin (in black) inserted between the two materials, which is part of the GAL separated from the PG. The GAL of the left-hand side is close to the PG. Note that the right-sided GAL separated during sample preparation (freeze-drying, cutting and/or polishing): the similarity between the GAL surface appearance of the right side with PG clearly supports this

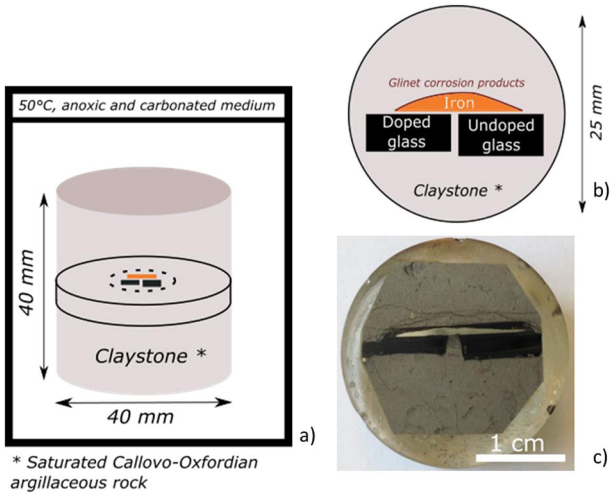

Fig. 1 Experimental setup of the glass/iron/claystone system. Arrangement of the two SON68 glass coupons pressed against a piece of iron in the Cox claystone cylinder (**a**), and cross section obtained on the system (**b** and **c**).

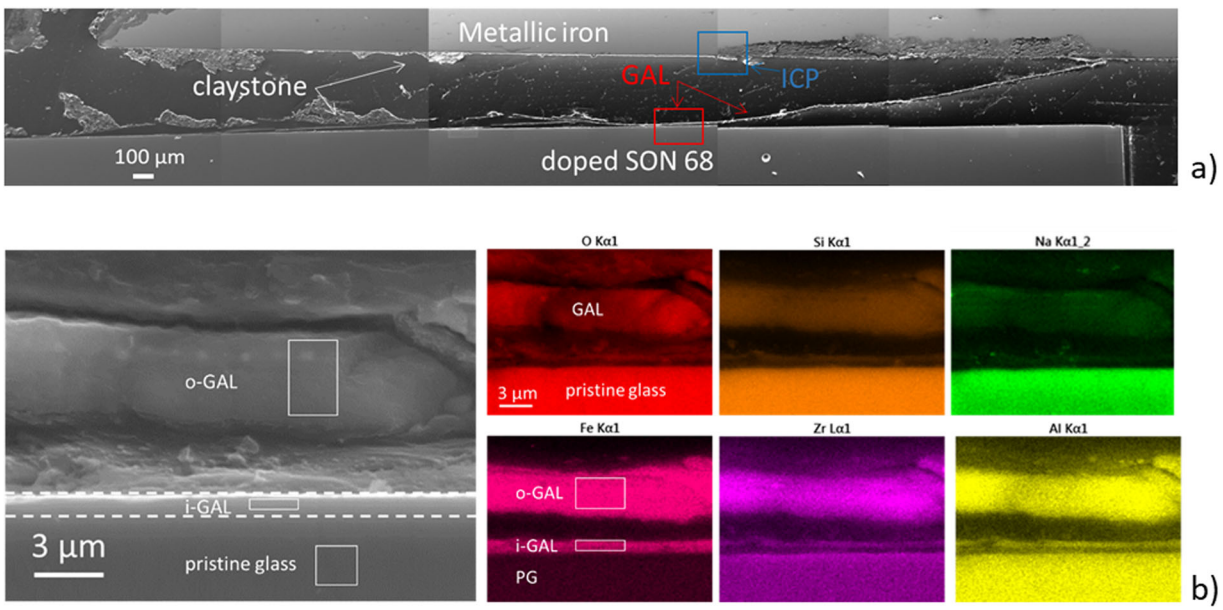

Fig. 2 SEM analyses at the glass/iron interface. a SEM micrograph of the doped nuclear glass/iron interface. The rectangles indicate the areas studied in detail (i.e., GAL and ICP). **b** SEM micrograph and EDS elemental mapping of the doped glass surface. White squares indicate areas of EDS analyses (Table 1).

hypothesis (see the SEM micrograph with the appropriate scale, Supplementary Fig. S1a).

Glass alteration layer characterization

Along the pristine glass specimen, SEM coupled with Energy Dispersive Spectroscopy (SEM-EDS) analyses show an inner and outer glass alteration layer, hereafter referred to as i-GAL and o-GAL, respectively (Fig. 2b). Both the i-GAL and o-GAL thicknesses are regular and measure 1 µm ($\sigma = 0.2$ µm, ten measurements) and 5 µm ($\sigma = 1$ µm, ten measurements), respectively (Fig. 2b). The main elements detected in the GALs and PG by SEM-EDS are shown in Table 1 and mapped in Fig. 2b. The GALs contain mainly Fe, Si, O, Al, and Zr. No Na was detected in the GALs (Na < detection limit of the EDS), and heavy elements such as Mo, Cs, Ba and lanthanides (La, Ce, Pr, Nd) are not detected. Conversely, PG contains 4.5 wt.% of Na and 10.5 wt% of the heavy elements. The Si/Zr ratio decreases by a factor of 2 in the GALs (4–5) compared to the PG (~10), mainly attributed to the Si content of the PG being twice that of the GALs, as the Zr content is similar since it is not soluble in water[2,9,42]. In contrast, GALs are enriched in Fe, as the Fe/Si ratios are equal to 0.1 and 2 in PG and GALs, respectively. Note that the incorporation of Fe in GALs has been already reported in previous studies[35,36,38,39,43]. Furthermore, the o-GAL sometimes corresponds to a stack of micrometric layers (Supplementary Fig. S1b), with a total thickness of 10 µm. Each layer has the same chemical composition as the one described hereafter.

Transmission Electron Microscopy (TEM) with Energy Dispersive Spectroscopy (TEM-EDS) analyses (Fig. 3a, b and c) show that the i-GAL consists of a stack of thin alteration layers of 0.2 µm (total 1–1.5 µm thickness), which are composed of foliated aggregates (Fig. 3c) compatible with the poorly-ordered smectite morphology[44]. Also pores are evidenced in the alteration layer, of the order of 10–50 nm in diameter, much larger than that observed in dense passivating GALs[10,45]. Note that the PG/i-GAL interface is precisely located by TEM-EDS due to the change in the Si/Zr ratio and Fe content (Fig. 3d). TEM analyses performed on the o-GAL shows the presence of crystallized sheets (Fig. 4), mainly composed of Si, Fe, O, Al (Table 2). High-resolution TEM (HRTEM) revealed characteristic morphology of well-ordered clay sheets, with reticular distances of 10.4 Å ($\sigma = 0.6$, 15 measurements) between the sheets (Fig. 4c), corresponding to the d_{001} distance. This value is compatible with partially dehydrated smectites[46–48], whose reticular distance could be modified through the freeze-drying preparation process.

Table 1. SEM-EDS composition ($\sigma < 0.5$) in wt.% obtained in pristine glass, in the inner and outer GAL (analyses performed in the white squares in Fig. 2b), and in the ICP (Fig. 7).

Element	PG	i-GAL	o-GAL	ICP without Si (left side)	ICP, needles (right side)	ICP with Si (right side)
O	44	39	36	33	32	33
Na	4.5	n.d.	n.d.	n.d.	n.d.	1
Al	3.2	5.2	5.5	n.d.	n.d.	n.d.
Si	26	17	18	n.d.	4	18
Ca	3.2	1.2	1	13	1	1
Fe	3.2	32	35	54	63	47
Zr	2.7	3.4	4.1	n.d.	n.d.	n.d.
Mo+Cs +Ba+La +Ce+Pr +Nd	10.5	0.4	n.d.	n.d.	n.d.	n.d.
Si/Zr	9.6	5.0	4.4	n.c.	n.c.	n.c.
Fe/Si	0.1	1.9	1.9	n.c.	n.c.	n.c.
Other elements	2.7	1.8	0.4	n.d.	n.d.	n.d.

(n.d. for not detected, n.c. for not concerned).

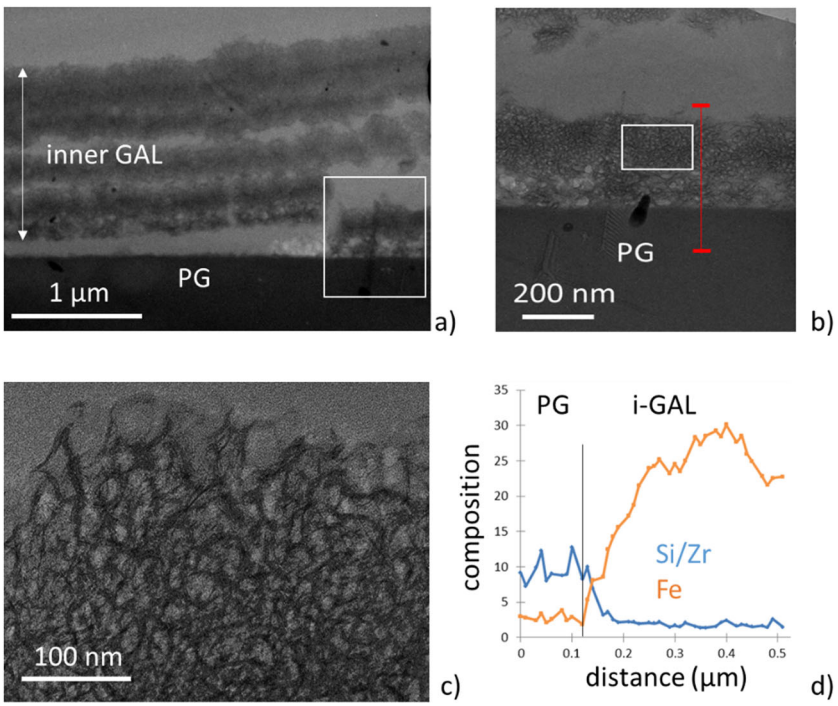

Fig. 3 TEM analyses performed in the inner GAL. a TEM micrographs of the i-GAL evidencing several strata and location of the profile composition (red line) in the first stratum (**b**). In **c**, HRTEM in the first stratum of the i-GAL showing foliated aggregates compatible with the smectite morphology. In **d**, TEM-EDS profile composition (wt.%) obtained in the first stratum of the i-GAL highlighting the PG/i-GAL interface.

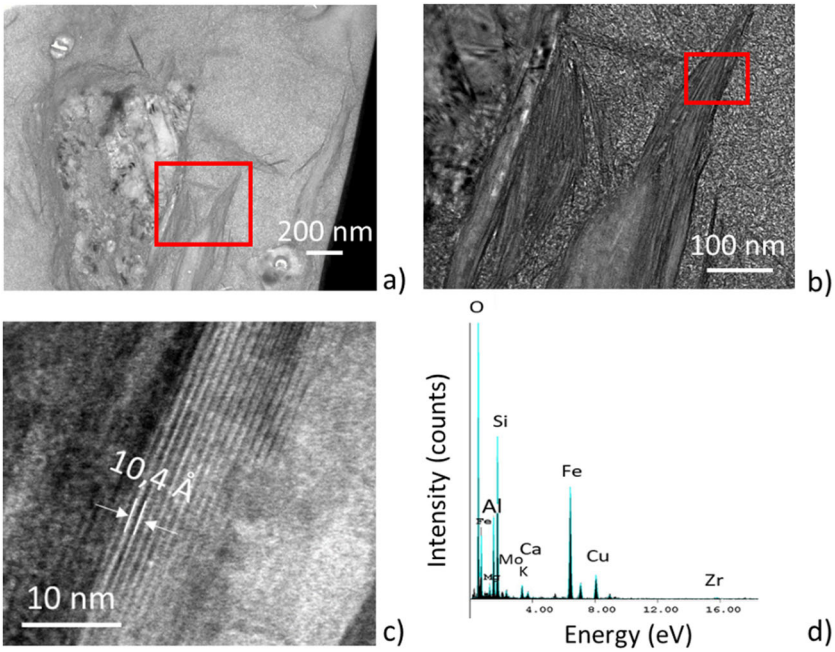

Fig. 4 TEM analyses in the o-GAL. High resolution TEM micrographs (**a** + **b** + **c**) highlighting the presence of crystalline phases with interreticular distance of 10.4 Å ($\sigma = 0.6$) compatible with smectite group. TEM-EDS spectrum (**d**) corresponding to the crystalline phase (composition in Table 2).

Table 2. TEM-EDS composition ($\sigma < 0.5$) in wt.% of the diffracted phase (red rectangles in Fig. 4).

O	Mg	Al	Si	Mo	K	Ca	Fe	Cu	Zr
39	1	6	15	3	2	1	26	6	1

Presence of Cu is only due to the support grid of the FIB foil.

Carrière et al.[37] demonstrated the possibility to identify nanometric silicates (crystallized or not) contained in glass matrix with Scanning Transmission X-ray Microscopy (STXM) at Si K and Fe L-edges. The same comparative approach is led for both edges using the same database of silicate reference spectra. STXM spectra at the Si K-edge from the PG, i-GAL and o-GAL are shown in Fig. 5a. For the PG, the spectrum is characteristic of amorphous SiO_2 ($SiO_{2(am)}$)[37]. Spectra obtained from the i-GAL and o-GAL differ from that of the PG, also having peaks B and C at around 1850 and 1855 eV, respectively. A qualitative comparison with the Si K-edge database supports the presence minerals from the smectite group (peaks in A, C and D positions), and excludes the presence of minerals from chlorites, mica, and serpentines-kaolinite groups for the GALs. Linear combination fitting of the GALs spectra using the Si K-edge database suggests that the i-GAL is around 75% nontronite and 25% $SiO_{2(am)}$ (expressed in equivalent thickness) and that the o-GAL is about 90% nontronite and 10% $SiO_{2(am)}$ (Fig. 5b, Table 3). The higher content of $SiO_{2(am)}$ for the i-GAL than for the o-GAL is consistent with a less-ordered nontronite.

Fe L-edge spectra are used to assess the Fe valence state in the PG and GALs, and are presented in Fig. 5c. Linear combination fitting of the PG and GALs Fe spectra, using reference spectra from pure Fe(II) (siderite) and Fe(III) (maghemite) compounds[49–52], are shown in Table 4. The Fe valence in PG is 100% Fe(III). On the contrary, mixed valence is observed in the GALs, 50% Fe(II) and 50% Fe(III) for i-GAL and 10% Fe(II) and 90 % Fe(III) for o-GAL. This Fe valence ratio corresponds to a well-ordered nontronite for the o-GAL[37], but for i-GAL the Fe valence ratio highlights a nontronite in formation, poorly ordered, as evoked by the calculated amorphous part (25%).

The SON68 glass was initially doped with ^{29}Si and ^{57}Fe - two isotopes at low concentration at the natural abundance (4.68% and 2.2%, respectively)—to monitor the distribution of these elements in the GAL, and thus better understand how this material forms. Note the i-GAL was divided into two parts (internal, adjacent to PG, and external) to extract the Time-of-Flight Secondary Ion Mass Spectrometry (ToF-SIMS) data. Table 5 presents the ToF-SIMS Si and Fe isotopic content after extraction of the mass spectra from the PG, i-GAL (internal and external), and o-GAL regions. ToF-SIMS analyses performed in the GAL of the undoped glass (right glass in Fig. 1) does not evidence any ^{29}Si enrichment (results not shown here), i.e., Si isotopic contents correspond to the natural abundance of the primal glass matrix. This strongly suggests that the two compartments of the experimental cell can be considered as isolated without interactions. The undoped compartment is not considered further in the rest of the paper. Note also that the $^{30}Si^+$ and $^{54}Fe^+$ contents correspond to the natural abundance and are not discussed hereafter[53].

An overlay mapping of $^{56}Fe^+$ and B^+ ions is represented to localize at the submicrometric scale the PG/i-GAL interface (Fig. 6b). Indeed, boron is only present in PG, as it is one of the first element to solubilize while glass alters[9,40]. On the contrary, $^{56}Fe^+$ is quasi-exclusively present in GAL (Fig. 6a, Table 5) and comes from another source (corrosion of iron, see ICP characterization part). PG contains 52% and 45% of $^{29}Si^+$ and $^{28}Si^+$, respectively, similar to that of the internal i-GAL. There is a slight enrichment in the $^{28}Si^+$ content in the external i-GAL (54%) compared to the internal i-GAL (46%). The Cox water initially contains silicon in the following proportions: ^{28}Si (92.2%), and ^{29}Si (4.7%) in accordance with the natural abundance[53]. This suggests that some of the Si in the external i-GAL originates from the Cox water. The $^{29}Si^+$ and $^{28}Si^+$ isotope content measured in the o-GAL is 20% and 78%, respectively, considerably different from that of the PG and i-GALs. Thus, a good portion of the Si content in the o-GAL originates from the Cox water. The origin of the Si in the

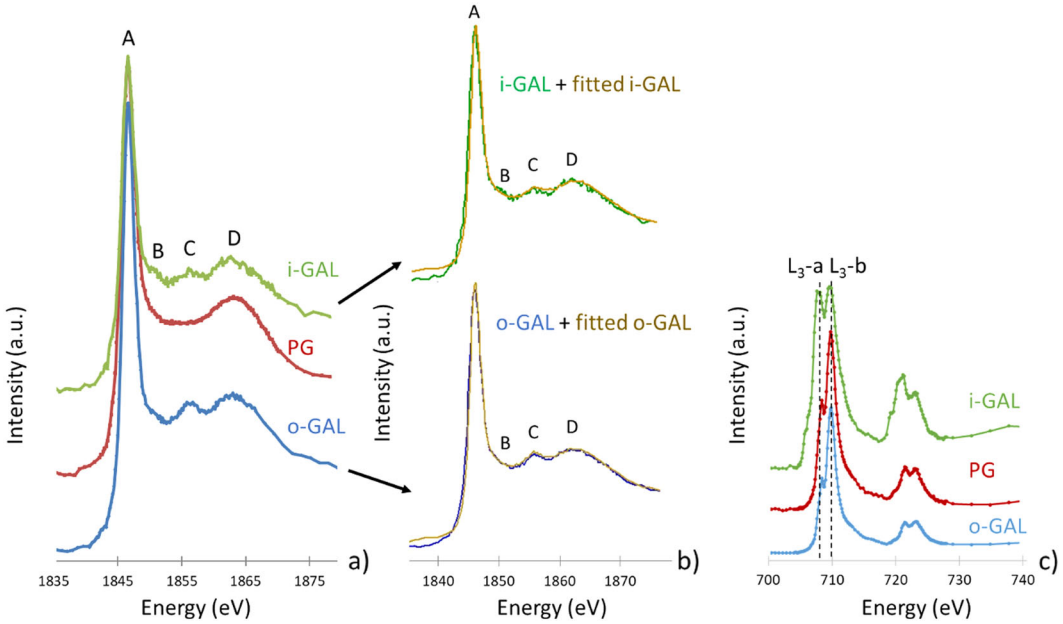

Fig. 5 STXM analyses at Si K and Fe-L edges of the glass alteration layer. a Si K-edge spectra obtained in pristine glass, i-GAL and o-GAL and superposition of i-GAL and o-GAL spectra with corresponding fitted spectra (**b**). Fe L-edge spectra obtained in pristine glass, i-GAL and o-GAL (**c**).

Table 3. Decomposition of the STXM spectra at Si K-edge obtained in i-GAL, in o-GAL (Fig. 5) and in ICP (Fig. 7f) containing silicon (right side, Fig. 2a).

Spectra	Decomposition (±2)	R^2	Chi²
i-GAL	74% nontronite + 26% amorphous SiO_2	0.98	0.004
o-GAL	88% nontronite + 12% amorphous SiO_2	0.99	0.015
ICP	97% nontronite + 3% amorphous SiO_2	0.99	0.04

Table 4. Valence of iron at nanometer scale (±2) in pristine glass, i-GAL and o-GAL obtained with linear regression on Fe L-edge spectra.

spectra	Fe(III)	Fe(II)
PG	100 %	0 %
i-GAL	50 %	50 %
o-GAL	90 %	10 %

external i-GAL and in the o-GAL could be estimated precisely assuming the following equations Eqs. (1) and (2):

$$^{29}Si_{GAL} = x_{PG} \times {}^{29}Si_{PG} + y_{sol} \times {}^{29}Si_{sol} \quad (1)$$

$$^{28}Si_{GAL} = x_{PG} \times {}^{28}Si_{PG} + y_{sol} \times {}^{28}Si_{sol} \quad (2)$$

where $^{29}Si_{PG}$ and $^{29}Si_{sol}$ correspond to the isotope content of ^{29}Si originating from the PG and Cox solution respectively, and the percentage of $^{29}Si_{PG}$ and $^{29}Si_{sol}$ are noted x_{PG} and y_{sol}, respectively. $^{29}Si_{GAL}$, $^{28}Si_{GAL}$, $^{29}Si_{PG}$ and $^{28}Si_{PG}$ correspond to the isotopic contents estimated by ToF-SIMS and $^{29}Si_{sol}$ and $^{28}Si_{sol}$ are related to the natural abundance. Solving this system yields that about 85% of Si contained in the external i-GAL comes from the glass, and 15% from the solution. Regarding o-GAL, about one third of Si (32%) comes from the glass, and two thirds from solution (68%).

Table 5. ToF-SIMS isotope content in percent (±2 for Si contents, ±0.2 for Fe contents) from the PG, i-GAL (internal and external), o-GAL (regions identified by the white rectangles from Figs. 2b and 6), and from ICP containing silicon (right side).

Isotope content	PG	i-GAL (internal)	i-GAL (external)	o-GAL	ICP with Si
$^{28}Si^+/\Sigma Si^+$	45	46	54	78	78
$^{29}Si^+/\Sigma Si^+$	52	53	45	20	19
$^{30}Si^+/\Sigma Si^+$	3	1	1	2	3
$^{57}Fe^+/\Sigma Fe^+$	96	50	19	3	3
$^{56}Fe^+/\Sigma Fe^+$	3	49	76	91	92
$^{54}Fe^+/\Sigma Fe^+$	1	1	5	6	5

Most of the Fe in the PG corresponds to the ^{57}Fe (96%). On the contrary, the internal i-GAL contains 49% of ^{56}Fe, coming from corrosion of the iron metal (discussed thereafter). The external i-GAL is further enriched with $^{56}Fe^+$ (76%) and the o-GAL is almost entirely ^{56}Fe (91%), close to the Fe natural abundance[53]. Thus, Fe migrated from the iron metal toward the glass surface.

Iron corrosion product characterization

The ICP on the left-hand side of the metallic part (Fig. 2a) were investigated with SEM-EDS and Raman spectroscopy (Fig. 7a, b, and c). On this side, the ICP layer is about 5 µm thick ($\sigma = 1$ µm, 20 measurements), with a maximum value of 10 µm. Only O, Fe, and Ca are detected in the ICP (Fig. 7b and Table 1). µRaman spectra (Fig. 7c) obtained at this location show two typical vibration bands at 281 and 1082 cm^{-1}, attributed to siderite ($FeCO_3$)[54,55]. Previous research of iron corrosion in carbonated and anoxic environments showed that ICP are formed by precipitation of aqueous carbonates with Fe(II), and are associated with generalized corrosion[35,37,39,43,52,56–60]. ICP on the right-hand side of the metallic zone are thicker, with an average thickness of about 100 µm ($\sigma =$ 10 µm, 15 measurements), reaching a thickness of 140 µm in

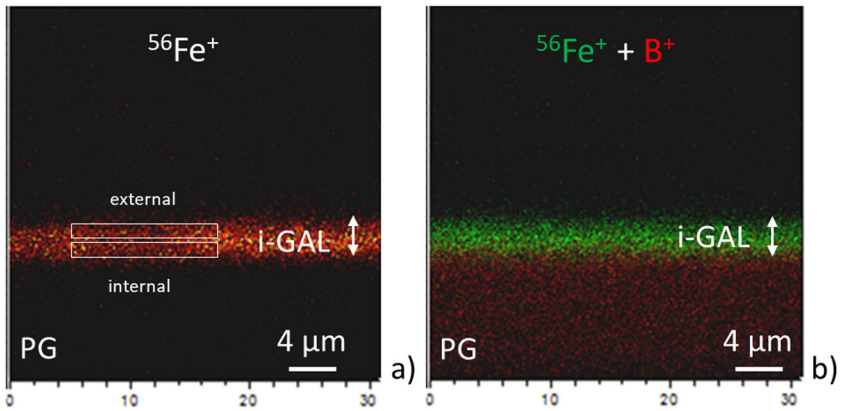

Fig. 6 ToF SIMS positive ion images obtained at the PG/i-GAL interface. ToF-SIMS image of $^{56}Fe^+$ (**a**) and overlay of $^{56}Fe^+$ and B^+ maps (**b**).

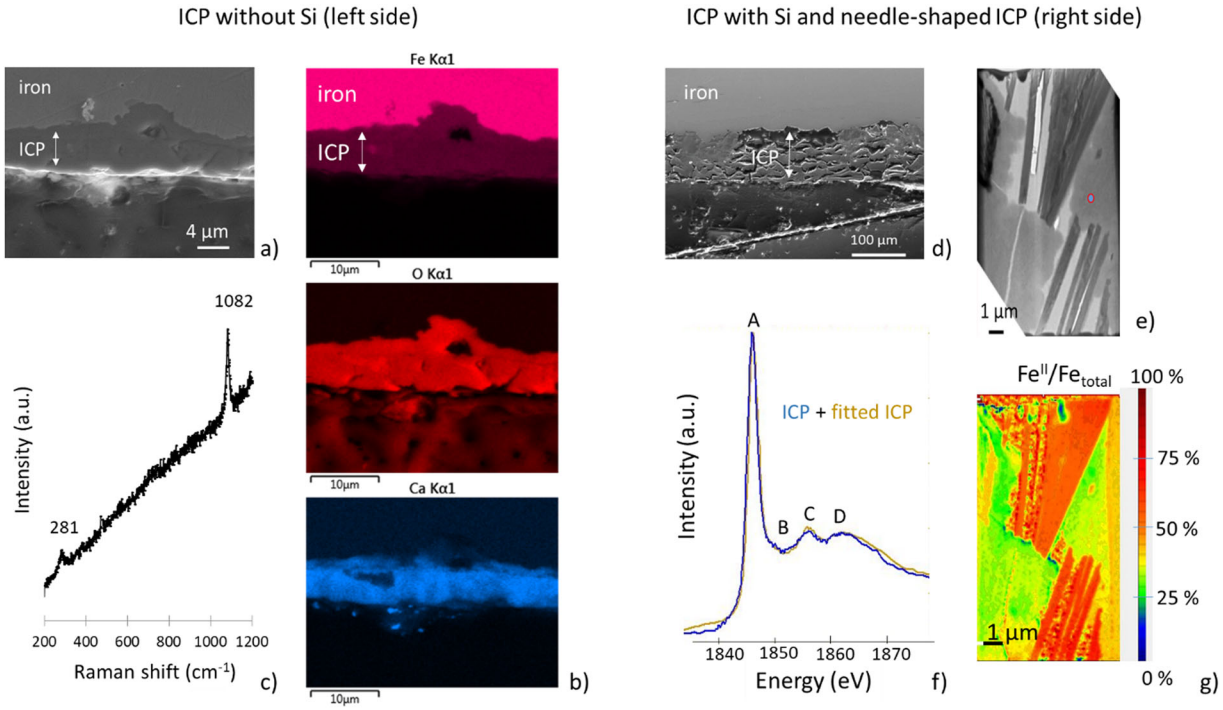

Fig. 7 ICP characterizations. a SEM micrograph, **b** SEM-EDS elemental mapping and **c** µRaman analyses of ICP on the left side, without Si. **d** SEM micrograph and **e** TEM micrograph of ICP on the right side, i.e., containing Si or needle-shaped ICP. **f** STXM spectra at Si K-edge on ICP with silicon (blue) and fitted spectrum (brown). **g** quantitative Fe redox nanomapping obtained with STXM at Fe L-edge from micrograph in **e**.

some areas. Two types of corrosion products are detected at this location. The first one seems crystalized with a needle shape (Fig. 7d and e) and contains mainly O and Fe (63%) (Table 1), with a small amount of Si (4%), while the second ICP contains more Si (18%) and less Fe (47%) and few quantities of Na and Ca (1%) (Table 1). Raman Spectroscopy identifies an iron carbonate, chukanovite $Fe_2(OH)_2CO_3$ (Supplementary Fig. S2)[61], corresponding to the needles. However it was not possible to identify the Si-containing ICP with this technique due to high fluorescence.

ToF-SIMS was performed on the second ICP containing high silica to determine the origin of the Si (Table 5). The Si isotope contents are very similar to that observed for o-GAL, i.e., 19% and 78% for $^{29}Si^+$, and $^{28}Si^+$ respectively, which suggests that one third of the Si contained in ICP comes from the glass, and two thirds from the solution, based on GAL analysis, Eqs. 1 and 2. These ICP contain amounts of $^{57}Fe^+$ and $^{56}Fe^+$ ions similar to the iron metal, (meaning natural abundance of Fe)[53] and not from the ^{57}Fe doped PG. Therefore, negligible Fe in the ICP came from the glass alteration.

STXM analysis at the Si K-edge was carried out on the ICP to identify the Si-containing phases. Only one Si species was apparent in the ICP with high Si (between the needles—in blue, Fig. 7f). Based on the spectrum shape, it is characteristic of smectites[37]. Linear combination fitting of the Si K-edge spectrum (Fig. 7f) using reference spectra from our library indicates that the Si species is nontronite (97%), with a small amount of SiO_2 (3%) (Fig. 7, Table 3). Note that the presence of SiO_2 could be caused by the amorphization of each faces of the FIB foil during sample preparation[62,63]. Contrary to the nontronite identified in the o-GAL, this one is poorly crystallized (diffused rings on the selected area electron diffraction pattern in Supplementary Fig. S3). STXM at Fe L-edge is sensitive to the iron valence[49,50,64]. Fig. 7g displays an Fe(II)/∑Fe nanomapping obtained with STXM at Fe L-edge, according to the procedure described by

Bourdelle et al.[49]. The needles displayed in red have an Fe(II)/∑Fe close to 80%, while Si containing phases, identified as nontronite, features an Fe(II)/∑Fe close to 20%. These values correspond to those expected for chukanovite and nontronite respectively, with an obvious bias of Fe valence as these two phases may overlap.

DISCUSSION

Our study shows that glass alteration at 50 °C, in close proximity to iron metal, in an anoxic clayey environment forms Na-free, Si-depleted and Fe-rich alteration layer. This GAL consists of a stack of many sublayers parallel to the glass surface, with a total thickness ranging from 6 to 10 µm. Authors usually interpret the depletion of Na by ion-exchange between protons dissociated from water molecules with alkalies acting as glass modifiers (Na, Li…)[8,34,65]. Moreover, a decrease in the Si/Zr ratio by a factor of two from the PG attests to a significant release of Si from the glass, suggesting that hydrolysis of the silicate network drives the alteration of the glass[2,66]. In general, ion-exchange, hydrolysis and condensation reactions lead to the formation of an amorphous hydrated layer on the glass surface, called gel, whose transport-limiting capability depends on the density of the material[16,67–69]. Highly protective gels are characterized by a high retention factor of Si and the presence of micropores poorly connected together[45,70]. However, in the present study, ordered precipitates of an Fe(III)-rich phyllosilicate, nontronite, belonging to the smectite group of clay minerals, forms at the glass surface, with pore sizes ranging from 10 to 50 nm in the layer closest to the glass (i.e., i-GAL) (Fig. 3). The nontronite constituting the porous i-GAL takes up a majority of the silicon released by the glass (H_4SiO_4), while the long-ordered nontronite (o-GAL) uses mainly the silicon from the solution (i.e., Cox water). Even though the solution composition was not analyzed at the end of the experiment (i.e., 2.5 yr), the $^{29}Si/^{28}Si$ ratio in the ordered nontronite is presumably close to the solution in equilibrium with claystone containing also hydrolyzed silicon. Hence the observations suggest that: i) the GAL is not or poorly protective, and ii) a dissolution/reprecipitation mechanism controls glass alteration under the study conditions.

In the present study, the alteration conditions (1 bar, 50 °C, neutral pH in an anoxic and carbonated medium) correspond to the geochemical environment favorable for nontronite precipitation[46,71–78]. However temperature has a strong influence on iron silicate formation. Indeed, iron/claystone or glass/iron/claystone experiments performed at 90 °C showed that serpentine formation occurs, whereas a temperature close to 50 °C tends to destabilize serpentine[35,48,56,57,79–84]. This could explain the absence of serpentine in our study. Moreover, saponite (belonging to the smectite group of clay minerals) is not observed here since it contains mainly Fe(II) and preferentially precipitates at higher pH than nontronite[76,85–87].

Despite initial reducing conditions, nontronite contains mostly Fe(III), as already shown in this iron phyllosilicate[88,89]. The literature suggests that iron oxidation from Fe(II) to Fe(III) in reducing conditions could be explained by water reduction[71,90,91], but could also result from a charge transfer or charge compensation within the silicate structure[77,92]. Another explanation would be to consider the glass as an oxidizer. Fe^{2+} coming from iron corrosion, and adsorbed at the glass surface, could be oxidized in Fe^{3+} by Fe_2O_3 (i.e., an Fe(III) oxide) of the glass, while the Fe(III) of glass would be reduced. A redox front could form between pristine glass, nontronite and solution, with two Fe(III)-rich ends, i.e., pristine glass and nontronite in contact with the solution, and a Fe^{2+}/Fe^{3+} gradient between glass and nontronite. This hypothesis requires further investigations.

As a reminder, the GAL consists of a succession of several nontronite strata (Fig. 3 and Supplementary Fig. S1). These observations were already modeled[93], suggesting a mechanism by cyclic locally pH modification. Indeed, glass dissolution rises the pH by releasing sodium or boron into solution[94,95], while smectite precipitation tends to decrease the pH, by consuming hydroxyl groups contained in solution[75], and releasing protons[96–98]. Moreover, redox variations cannot be excluded to justify these strata.

To estimate glass alteration rates, quantification of boron in leaching solution is commonly used[9]. Unfortunately, the solution could not be periodically sampled as the reactor remained a closed system for the whole duration of the experiment. Previous studies have shown that the GAL thickness could be used to estimate glass alteration rates[40]. This method assumes the glass alteration to be isovolumetric. In aggressive conditions such as used in this study (i.e., glass in contact with iron) some researchers consider that the glass alteration is isovolumetric[35,99], while others describe it as non-isovolumetric due to the incorporation of Fe in the GAL and to glass density modification[18,100]. Consequently, the alteration rate calculated from the GAL thickness could be over or underestimated. Nevertheless, it was established that the difference between these two calculation methods was a factor of two, when silicon retention in a gel, named *f(Si)*, is low (<15%)[9]. Another method, based on the *f(Si)* in the GAL, is proposed in this paper for a complementary estimation of the mean alteration rate.

In this study, the average rate of glass dissolution is estimated at 1.8×10^{-2} g m^{-2} d^{-1} to 3.0×10^{-2} g m^{-2} d^{-1}, for a GAL thickness of 6–10 µm, respectively, assuming a constant dissolution rate and an isovolumetric process. This is five to three times lower than the initial dissolution rate of SON68 glass measured in previous experiments in synthetic Cox poral fluid at 50 °C, referred to as $r_{0\,Cox}^{50°C} = 9.3 \times 10^{-2}$ g m^{-2} d^{-1}. However, it is several orders of magnitude higher than the residual rate (r_r) estimated at around 6×10^{-5} g m^{-2} d^{-1} at 50 °C[101,102].

A second estimation of the alteration rate can be made from the retention factor of Si, *f(Si)*, in the GAL. As Zr is supposed to remain undissolved according to previous studies[2,9,42], silicon retention obtained with Eq. 3 enables the estimation of the alteration rate[103].

$$f(Si) = \frac{Si/Zr_{in\,GAL}}{Si/Zr_{in\,PG}} \quad (3)$$

Two empirical curves (Fig. 8) showing glass alteration rate in pure water at 50 °C vs *f(Si)* (Fig. 8a) or vs $[H_4SiO_4]$ in solution (Fig. 8b) were drawn from literature data (Supplementary Table S1)[104,105]. To our knowledge, these values do not exist in literature for glass alteration in Cox water. Therefore this method is used to approximate the alteration rate and complements the first method. Looking in detail at the curve, from *f(Si)* = 0–0.6, the glass dissolution rate is divided by 10. From 0.6 to maximal Si retention at 0.8, the rate reaches $r_0/1000$, due to the formation of a protective gel at the glass surface. The Si retention factor calculated for the GAL, i.e., 0.5 in the present study, suggests that hydrolyzed Si is partially retained in the altered layer. The glass alteration rate associated with these value is 1.6×10^{-2} g m^{-2} d^{-1}, and is in fair agreement with the rate obtained from GAL thickness (i.e., $r_{0\,Cox}^{50°C}/5$).

Alteration rate calculated from this second method yields a mean concentration of H_4SiO_4 in the leachate of 6.2×10^{-5} mol l^{-1} (Fig. 8b). This concentration is far from saturation with a protective gel (about 10^{-3} mol l^{-1})[21–26]. The glass alteration rate can be determined using Eq. (4), where $k^+ = 1.2.10^8$g.m^{-2}.d^{-1} is the kinetic constant in pure water, $n = -0.4$ the coefficient of the pH-dependence of the reaction rate, $Ea = 77$ kJ mol^{-1} the activation energy of the glass dissolution reaction, a_{H4SiO4} the H_4SiO_4 activity in solution, and K the solubility constant of the protective gel (corresponding to amorphous silica)[2,66]. Hence a concentration of 6.2×10^{-5} mol l^{-1}of H_4SiO_4 in solution lead to a dissolution rate

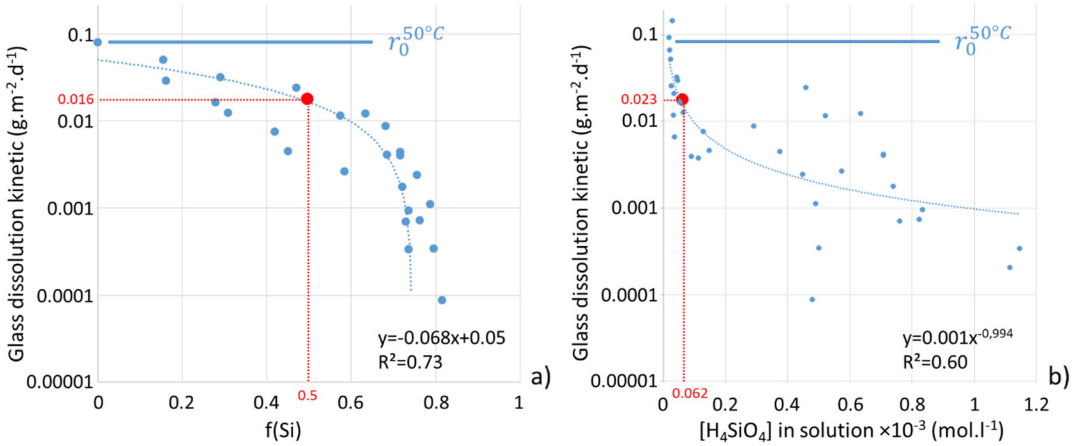

Fig. 8 Estimated glass dissolution kinetics in function of silicon retention (f(Si)) or H_4SiO_4 concentration in solution. According to the f(Si) = 0.5 in GAL and the $[H_4SiO_4] = 0.062$ mol l^{-1} in solution, the glass alteration rates associated with these values are respectively 1.6×10^{-2} g m^{-2} j^{-1} (**a**) and 2.3×10^{-2} g m^{-2} j^{-1} (**b**).

estimated at 2.3×10^{-2} g m^{-2} d^{-1}, i.e., $r_{0\,Cox}^{50\,°C}/4$, with the Eq. (4).

$$r = k^{+} a_{H^{+}}^{n} e^{-\frac{Ea}{RT}} \left(1 - \frac{a_{H_4SiO_4}}{K}\right) \quad (4)$$

The two methods used to estimate the glass alteration rate give consistent results. Glass alters at a high rate, releasing large amount of Si, which then co-precipitates with Fe. It can then be proposed that the presence of Fe in the vicinity of glass favors a mechanism of dissolution/reprecipitation instead of the formation of a passivating layer by in-situ reorganization of the silicate network.

The affinity between Si and Fe was evidenced with concentration diagram calculated with the physicochemical alteration conditions, i.e., temperature of 50 °C, atmospheric pressure, redox conditions of −0.14 V vs.SHE, Cox water composition (Supplementary Table S2). Phases observed experimentally in this study (mainly nontronite, and small amounts of amorphous silica $SiO_{2(am)}$) were included in the model (see "Methods"). Figure 9 illustrates the predominance domains of precipitate phases (in yellow) of $nontronite_{(s)}$ and $SiO_{2(am)}$. The activities of the H_4SiO_4 and the ratio Fe^{2+}/Fe^{3+}, are the two variables that control the formation and stability of the main phases observed in the system. The Fe^{2+}/Fe^{3+} ratio was calculated using Nernst equation. Al is required to form nontronite. Although its concentration in solution is not known, it was fixed at 4.6×10^{-6} mol l^{-1} in the simulation. This concentration corresponds to the amount of Al in solution assuming that Al and Si are dissolved congruently from the glass. It has been verified that the activity diagrams are not modified for an order of magnitude smaller and higher than our Al concentration (not shown).

At pH = 6.9, the blue and red lines in Fig. 9 indicate the initial H_4SiO_4 concentration in Cox solution in equilibrium with claystone, and the estimated concentration of 6.2×10^{-5} mol l^{-1} deduced from Fig. 8, respectively. It suggests that these concentrations are high enough to form nontronite, but do not allow $SiO_{2(am)}$ to form. Because the protective gel has a solubility product close to that of $SiO_{2(am)}$, this result strongly suggests that, in the studied conditions, the presence of iron in solution delays or prevents the formation of a protective gel, reinforcing the idea that glass alters following a dissolution/reprecipitation process. However, it must be kept in mind that a small fraction of $SiO_{2(am)}$ was also evidenced in the GAL, in addition to nontronite. This amorphous part was attributed to nontronite in formation, but it could also result from a local iron depletion at the vicinity of glass. Indeed, local iron concentration can decrease as nontronite precipitates, leading to an increase of *[H_4SiO_4]* due to glass alteration. Presumably saturation condition can be reached locally to form $SiO_{2(am)}$, i.e., a gel, until iron arrival to the glass and resumption of nontronite precipitation.

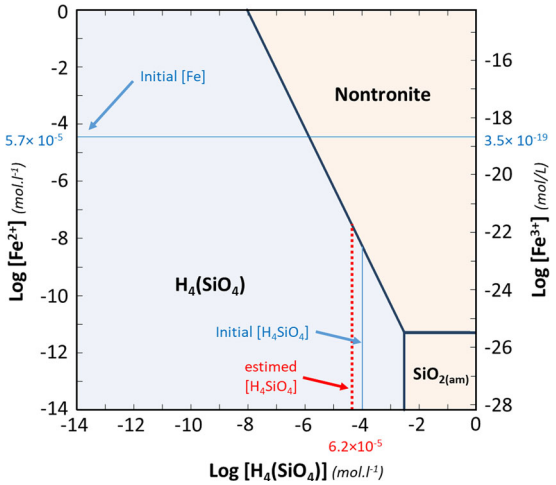

Fig. 9 Concentration diagram indicating stability of the main phases in the altered glass/iron/claystone system at 50 °C. Eh = −0.14 V vs. SHE and pH = 6.86 at atmospheric pressure. In blue dissolved species, and in yellow stability domains of nontronite and amorphous silica ($SiO_{2(am)}$). Blue lines present initial concentration of Fe and H_4SiO_4 in solution. Red line shows the concentration of H_4SiO_4 estimated in solution from Fig. 8b.

Owing to the high affinity between Si and Fe, and the low solubility limit and high precipitation rate of nontronite in our conditions, such porous phase forms at the expense of a protective gel. However it cannot be excluded that gradients of chemical species could appear near the surface of the glass, allowing some gel to form.

In the present study, the glass was altered by the solution in contact with steel and claystone. Owing to the high Si/Fe affinity, both Si released by the glass and that present in the pore water, precipitate with the aqueous Fe(II) species coming from steel corrosion to form Fe(III)-rich smectite layer (assimilated to nontronite), as illustrated in Fig. 10. Near the glass surface, a thin poorly-ordered and non-protective nontronite layer starts to precipitate mainly from species coming from glass dissolution. This material was associated to amorphous silica in the STXM spectrum deconvolution, but it does not relate to the protective gel described in other studies conducted in the absence of Fe. In the present work, we demonstrate that Fe prevents or delay the formation of a protective gel. As a consequence of nontronite

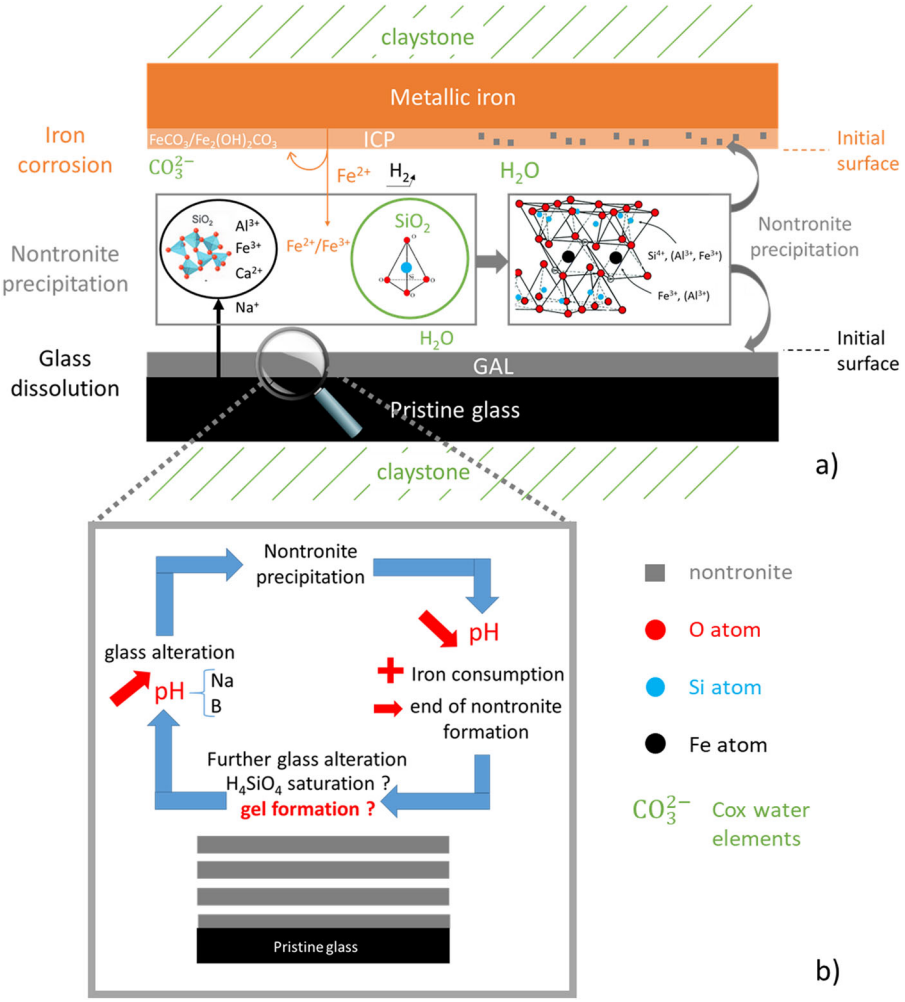

Fig. 10 Scheme of the glass alteration mechanism by dissolution/precipitation in the presence of iron corrosion and claystone. **a** Overview of such a mechanism, and **b** illustration of cyclic pH modifications leading to GAL consisting of several strata. SiO_2 tetrahedrons from the glass and nontronite structure drawn respectively by Calas et al.[118]. and Bailey et al.[119].

formation, glass alters following a dissolution/reprecipitation mechanism, likely limited by glass dissolution[31].

It remains to be seen whether such a precipitated nontronite layer could serve as a barrier limiting exchanges at the glass/solution interface. A recent study evidences that both glass alteration mechanisms, i.e., dissolution/precipitation and hydrolysis/condensation can lead to a pore closure, reducing water diffusion through the GAL[10]. Indeed, a precipitated layer can be protective, slowing down water transport. Hence, in their experimental conditions, authors conclude that the two mechanisms are not systematically antagonistic. It seems to depend on the geochemical conditions, and thus of the Fe-silicate group formation and stability in such conditions[106–108]. Furthermore, local and cyclic concentrations evidenced in the present study, and pH/potential modifications are likely to initiate a gel formation, even though Fe in solution behaves as a silicon pump under our conditions.

METHODS

Glass/Iron/claystone system

The glass/iron/claystone system reactor consists of a cylindrical core ($\Phi \sim 4$ cm, $L \sim 4$ cm) of Cox claystone, sampled from the Underground Research Laboratory of Bure (URL), cut into two half-cylinders and machined in order to place in the middle two coupons of SON68 glass (composition in Supplementary Table S3), pressed against a 1 mm thick piece of iron (Fig. 1). 400 µm separates the coupon and the piece of iron. One of the glass coupons is initially doped with ^{29}Si (55 wt%) and ^{57}Fe (100 wt%) to follow the migration of these two elements, while the other is not doped. Dimensions of doped glass and nondoped glass are respectively 10 mm × 10 mm × 2 mm and 20 mm × 10 mm × 5 mm (height × width × thickness). The iron (low alloy steel mainly ferritic) piece is prepared from a 450 yr old nail recovered from corrosion products (the Glinet archeological site, Normandy), such that pristine iron is on one face and on the opposite face is Glinet iron corrosion products. The pristine iron face is placed adjacent to the doped and undoped PG, butt-ended to each other. The undoped glass is used for reproducibility, and same analyses are performed on both glass coupons. The aim of Glinet corrosion products in contact with claystone is to limit the reactivity and flux of iron at the iron/claystone interface since old corrosion products are stable and less reactive than a "fresh" surface of iron[39,58]. Once assembled the reactor is placed in a membrane and resaturated with the deoxygenated synthetic Cox water (Supplementary Table S2) under 26 bar of pressure to rehydrate the medium and eliminate the gaseous oxygen present in the reactor[38]. The reactor is placed vertically and water circulation is from bottom to top. The system is closed once it is resaturated, then the water circulation is stopped. The system is aged in an oven at 50 °C for 2.5 yr, after which the system is frozen and lyophilized to eliminate water, embedded in a bi-component epoxy resin (Epothin Epoxy Buehler™) and then hot mounted in a tri-component Flucka resin at 40 °C under vacuum. This fluidized second resin enabled impregnation to the core of the system. The embedded system is then cut and polished down to 1 µm roughness under a N_2 atmosphere in a glove box to prevent oxidation. Cross section obtained at the doped glass/iron interface is presented in Fig. 2a.

Analytical techniques

Cross section, and especially the doped SON68 glass/metal iron interface is observed and characterized at different scales (macro-micro-nano) using different analytical techniques.

Scanning electron microscopy coupled with dispersive energy spectroscopy (SEM-EDS) was performed on a Jeol JSM-7001 F Field Effect at 15 kV and a beam time current of 12 nA. A carbon-coating layer of 15 nm was applied on the sample surface before analyses.

MicroRaman spectroscopy was carried out on an Invia Renishaw microspectrometer equipped with a doubled Nd-YAG laser at an excitation wavelength of 532 nm, and equipped with a CCD detector. The spatial resolution was about 1 μm^3 with the 50× lens. The laser power was filtered down to 0.5 mW and spectra were recorded for 30 sec with a resolution of 2 cm^{-1}. Spectra obtained in ICP are acquired and processed with the Wire 3.4 software.

Time-of-flight secondary ion mass spectrometry (ToF-SIMS), led on a TOF.SIMS 5 spectrometer (IONTOF, Munster, Germany) provides information on the migration of Si and Fe during glass and iron alteration (reminder: one SON68 coupon was initially doped with ^{29}Si and ^{57}Fe). Pulsed Bi^+ are used as primary ions (25 kV) in burst mode, i.e., ion beam is emitted with a series of short pulses to avoid detector saturation[109,110], enabling good mass resolution (up to 7000) and a good lateral resolution (up to 200 nm). This technique as also a high sensitivity with a detection threshold in the range of ppb. Positive ions ToF-SIMS images (Supplementary Fig. S4) are recorded in the regions of interest. Then isotopic contents are calculated from the mass spectra reconstructed from the selected areas.

Cross sections of 100 nm and 1 µm thick are cut in the regions of interest in the glass/iron/claystone system (i.e., mainly GAL and ICP) using a FEI Helios Nanolab 660 scanning electron microscope/focused ion beam (SEM-FIB). The acceleration voltage is from 0.5 to 30 kV and ion current from 1 pA to 65 nA. A "cleaning" at 5, 2, and 1 kV of the two faces of the FIB foils punctuates the preparation to eliminate the layer of damage and contamination.

To identify iron-silicate formed on GAL and ICP at nanometer scale, X-ray microscopy (STXM) imaging and spectroscopy is carried out on the spectromicroscopy (SM) beamline 10ID-1 at the Canadian Light Source (Saskatoon, Canada). Image sequences (stacks) of Near-Edge X-ray Absorption Fine Structure are collected on 100 nm and 1 µm thick cross sections at the Fe L- and Si K-edges, respectively. The measured transmitted signals (I) are converted into absorbance values using the incident flux (I_0) measured in the absence of the sample. STXM at Fe L-edge is sensitive to the iron valence[49,50,64], and Si K-edge probes atomic environment and nanostructure around the absorber atom at a distance greater than 5 or 6 Å[111–114]. The spectra derived from the stacks are decomposed using a least squares method with standard reference spectra, from our Si K- and Fe L-edges database[37,115], normalized to an absolute linear absorbance corresponding to a phase thickness of 1 nm (expressed in optical density). Fe(II)/∑Fe nanomapping at Fe L-edge is conducted according to the procedure described by Bourdelle et al.[49]. Analyses and data processing are achieved with the aXis2000 software.

Transmission electron microscopy on FIB cross sections is performed for iron-silicate identification on the GAL using a Jeol 2010 F electron gun at 200 kV, equipped with a diode EDAX X-ray microanalysis for chemical analyses or electron diffraction. The d_{001}-spacing of silicate sheets are measured from the HRTEM images using ImageJ software. The error is around 0.05 Å due to pixel resolution.

Geochemical modeling

Thermodynamic modeling is performed with the Geochemist's Workbench 12.0 software and the thermodynamic database "Thermochimie v10a electron" of Andra. The Cox water composition is used as input to plot the activity diagrams, with the Act2 mode. This mode establishes the diagram of the most thermodynamically stable phases, considering different approaches (equilibrium dissolution, speciation, precipitation reaction)[116]. The phases observed experimentally are included in the model (i.e., nontronite, $SiO_{2(am)}$), and a small amount of aluminum is also added ($[Al] = 4.6 \times 10^{-6}$ mol.l^{-1}). Precipitated phases and species in solution are indicated in yellow and blue, respectively. The thermodynamic constants from the database and reactions used for the geochemical modeling are summarized in Supplementary Tables S4 and S5. Initial concentration of iron in solution at 50 °C was deducted from Gailhanou et al.[117].

DATA AVAILABILITY STATEMENT

The datasets generated and/or analyzed during the current study are available from the corresponding author upon reasonable request.

Received: 29 September 2020; Accepted: 9 March 2021;
Published online: 08 April 2021

REFERENCES

1. Andra. Safety Options Report—Operating Part (DOS-Expl). 521 (2016). https://international.andra.fr/sites/international/files/2019-03/Safety%20Options%20Report%20-%20Operations_2.pdf
2. Frugier, P. et al. SON68 nuclear glass dissolution kinetics: current state of knowledge and basis of the new GRAAL model. *J. Nucl. Mater.* **380**, 8–21 (2008).
3. Grambow, B. Nuclear waste glasses—how durable? *Elements* **2**, 357–364 (2006).
4. Vernaz, É. Y. Estimating the lifetime of R7T7 glass in various media. *Comptes. Rendus. Phys.* **3**, 813–825 (2002).
5. Gin, S., Jollivet, P., Tribet, M., Peuget, S. & Schuller, S. Radionuclides containment in nuclear glasses: an overview. *Radiochim. Acta* **105**, 927–959 (2017).
6. Jollivet, P., Gin, S. & Schumacher, S. Forward dissolution rate of silicate glasses of nuclear interest in clay-equilibrated groundwater. *Chem. Geol.* **330–331**, 207–217 (2012).
7. Advocat, T., Jollivet, P., Crovisier, J. L. & Del Nero, M. Long-term alteration mechanisms in water for SON68 radioactive borosilicate glass. *J. Nucl. Mater.* **298**, 55–62 (2001).
8. Bunker, B. C., Arnold, G. W., Day, D. E. & Bray, P. J. The effect of molecular structure on borosilicate glass leaching. *J. Non Cryst. Solids* **87**, 226–253 (1986).
9. Gin, S., Ribet, I. & Couillard, M. Role and properties of the gel formed during nuclear glass alteration: importance of gel formation conditions. *J. Nucl. Mater.* **298**, 1–10 (2001).
10. Gin, S. et al. A general mechanism for gel layer formation on borosilicate glass under aqueous corrosion. *J. Phys. Chem. C.* 124, 5123–5144 (2020).
11. Gin, S. et al. The controversial role of inter-diffusion in glass alteration. *Chem. Geol.* **440**, 115–123 (2016).
12. Geisler, T., Dohmen, L., Lenting, C. & Fritzsche, M. B. K. Real-time in situ observations of reaction and transport phenomena during silicate glass corrosion by fluid-cell Raman spectroscopy. *Nat. Mater.* **18**, 342–348 (2019).
13. Stroncik, N. A. & Schmincke, H. Evolution of palagonite: crystallization, chemical changes, and element budget. *Geochem. Geophys. Geosyst.* **2**, 45–88 (2001).
14. Hellmann, R. et al. Nanometre-scale evidence for interfacial dissolution–reprecipitation control of silicate glass corrosion. *Nat. Mater.* **14**, 307 (2015).
15. Ducasse, T. et al. Alteration of synthetic basaltic glass in silica saturated conditions: analogy with nuclear glass. *Appl. Geochem.* **97**, 19–31 (2018).
16. Cailleteau, C. et al. Insight into silicate-glass corrosion mechanisms. *Nat. Mater.* **7**, 978 (2008).
17. Donzel, N., Gin, S., Augereau, F. & Ramonda, M. Study of gel development during SON68 glass alteration using atomic force microscopy. comparison with two simplified glasses. *J. Nucl. Mater.* **317**, 83–92 (2003).
18. Reiser, J. T. et al. The use of positrons to survey alteration layers on synthetic nuclear waste glasses. *J. Nucl. Mater.* **490**, 75–84 (2017).
19. Jollivet, P. et al. Investigation of gel porosity clogging during glass leaching. *J. Non Cryst. Solids* **354**, 4952–4958 (2008).
20. Gin, S. et al. The fate of silicon during glass corrosion under alkaline conditions: a mechanistic and kinetic study with the international simple glass. *Geochim. Cosmochim. Acta* **151**, 68–85 (2015).
21. Ferrand, K., Abdelouas, A. & Grambow, B. Water diffusion in the simulated French nuclear waste glass SON 68 contacting silica rich solutions: experimental and modeling. *J. Nucl. Mater.* **355**, 54–67 (2006).
22. Gin, S. Protective effect of the alteration gel: a key mechanism in the long-term behavior of nuclear waste glass. *MRS Online Proc. Libr. Arch.* **663**, 207–216 (2000).
23. Gin, S. et al. Atom-probe tomography, TEM and ToF-SIMS study of borosilicate glass alteration rim: a multiscale approach to investigating rate-limiting mechanisms. *Geochim. Cosmochim. Acta* **202**, 57–76 (2017).
24. Icenhower, J. P. & Steefel, C. I. Experimentally determined dissolution kinetics of SON68 glass at 90 °C over a silica saturation interval: evidence against a linear rate law. *J. Nucl. Mater.* **439**, 137–147 (2013).
25. Neeway, J., Abdelouas, A., Grambow, B. & Schumacher, S. Dissolution mechanism of the SON68 reference nuclear waste glass: new data in dynamic system in silica saturation conditions. *J. Nucl. Mater.* **415**, 31–37 (2011).
26. Neill, L. et al. Various effects of magnetite on international simple glass (ISG) dissolution: implications for the long-term durability of nuclear glasses. *npj Mater. Degrad.* **1**, 1 (2017).

27. Fournier, M. et al. Effect of pH on the stability of passivating gel layers formed on international simple glass. *J. Nucl. Mater.* **524**, 21–38 (2019).
28. Fournier, M. et al. Glass dissolution rate measurement and calculation revisited. *J. Nucl. Mater.* **476**, 140–154 (2016).
29. Crovisier, J.-L., Advocat, T. & Dussossoy, J.-L. Nature and role of natural alteration gels formed on the surface of ancient volcanic glasses (Natural analogs of waste containment glasses). *J. Nucl. Mater.* **321**, 91–109 (2003).
30. Valle, N. et al. Elemental and isotopic (29Si and 18O) tracing of glass alteration mechanisms. *Geochim. Cosmochim. Acta* **74**, 3412–3431 (2010).
31. Grambow, B. Nuclear waste glass dissolution: mechanism, model and application. (1987).
32. Bouakkaz, R., Abdelouas, A., El Mendili, Y., Grambow, B. & Gin, S. SON68 glass alteration under Si-rich solutions at low temperature (35–90 °C): kinetics, secondary phases and isotopic exchange studies. *RSC Adv.* **6**, 72616–72633 (2016).
33. Verney-Carron, A. et al. Understanding the mechanisms of Si–K–Ca glass alteration using silicon isotopes. *Geochim. Cosmochim. Acta* **203**, 404–421 (2017).
34. Gin, S. et al. Origin and consequences of silicate glass passivation by surface layers. *Nat. Commun.* **6**, 6360 (2015).
35. De Combarieu, G. et al. Glass–iron–clay interactions in a radioactive waste geological disposal: an integrated laboratory-scale experiment. *Appl. Geochem.* **26**, 65–79 (2011).
36. Rébiscoul, D. et al. Glass-iron-clay interactions in a radioactive waste geological disposal: a multiscale approach. *MRS Proc.* **1518**, 185–190 (2013).
37. Carrière, C. et al. Use of nanoprobes to identify iron-silicates in a glass/iron/argillite system in deep geological disposal. *Corros. Sci.* **158**, 108104 (2019).
38. Burger, E. et al. Impact of iron on nuclear glass alteration in geological repository conditions: a multiscale approach. *Appl. Geochem.* **31**, 159–170 (2013).
39. Dillmann, P., Gin, S., Neff, D., Gentaz, L. & Rebiscoul, D. Effect of natural and synthetic iron corrosion products on silicate glass alteration processes. *Geochim. Cosmochim. Acta* **172**, 287–305 (2016).
40. Grambow, B. & Müller, R. First-order dissolution rate law and the role of surface layers in glass performance assessment. *J. Nucl. Mater.* **298**, 112–124 (2001).
41. Frugier, P., Minet, Y., Rajmohan, N., Godon, N. & Gin, S. Modeling glass corrosion with GRAAL. *npj Mater. Degrad.* **2**, 1–13 (2018).
42. Brendebach, B., Altmaier, M., Rothe, J., Neck, V. & Denecke, M. A. EXAFS study of aqueous ZrIV and ThIV complexes in alkaline CaCl2 solutions: Ca3 [Zr (OH) 6] 4+ and Ca4 [Th (OH) 8] 4+. *Inorg. Chem.* **46**, 6804–6810 (2007).
43. Michelin, A. et al. Silicate glass alteration enhanced by iron: origin and long-term implications. *Environ. Sci. Technol.* **47**, 750–756 (2012).
44. Grauby, O., Petit, S., Decarreau, A. & Baronnet, A. The nontronite-saponite series: an experimental approach. *Eur. J Mineral.* **6**, 99–112 (1994).
45. Ngo, D. et al. Spectroscopic ellipsometry study of thickness and porosity of the alteration layer formed on international simple glass surface in aqueous corrosion conditions. *npj Mater. Degrad.* **2**, 1–9 (2018).
46. Changela, H. & Bridges, J. Alteration assemblages in the nakhlites: variation with depth on Mars. *Meteorit. Planet. Sci.* **45**, 1847–1867 (2010).
47. Moore, D. M. & Hower, J. Ordered interstratification of dehydrated and hydrated Na-smectite. *Clays Clay Miner.* **34**, 379–384 (1986).
48. Mosser-Ruck, R. et al. Effects of temperature, pH, and iron/clay and liquid/clay ratios on experimental conversion of dioctahedral smectite to berthierine, chlorite, vermiculite, or saponite. *Clays Clay Miner.* **58**, 280–291 (2010).
49. Bourdelle, F. et al. Quantification of the ferric/ferrous iron ratio in silicates by scanning transmission X-ray microscopy at the Fe L2,3 edges. *Contrib. Mineral. Petrol.* **166**, 423–434 (2013).
50. Dynes, J. J. et al. Speciation and quantitative mapping of metal species in microbial biofilms using scanning transmission X-ray microscopy. *Environ. Sci. Technol.* **40**, 1556–1565 (2006).
51. van Aken, P. A., Liebscher, B. & Styrsa, V. J. Quantitative determination of iron oxidation states in minerals using Fe L2,3-edge electron energy-loss near-edge structure spectroscopy. *Phys. Chem. Miner.* **25**, 323–327 (1998).
52. Michelin, A. et al. Effect of iron metal and siderite on the durability of simulated archeological glassy material. *Corros. Sci.* **76**, 403–414 (2013).
53. Lide, D. R. CRC handbook of chemistry and physics, *internet version 2005*. (2005).
54. Bernard, M. C. et al. Analysis of corrosion products beneath an epoxy-amine varnish film. *Prog. Org. Coat.* **45**, 399–404 (2002).
55. Saheb, M. et al. Multisecular corrosion behaviour of low carbon steel in anoxic soils: characterisation of corrosion system on archaeological artefacts. *Mater. Corros.* **60**, 99–105 (2009).
56. Schlegel, M. L. et al. Metal corrosion and argillite transformation at the water-saturated, high-temperature iron–clay interface: a microscopic-scale study. *Appl. Geochem.* **23**, 2619–2633 (2008).
57. Schlegel, M. L. et al. Corrosion of metal iron in contact with anoxic clay at 90 C: characterization of the corrosion products after two years of interaction. *Appl. Geochem.* **51**, 1–14 (2014).
58. Leon, Y. et al. Interfacial layers at a nanometre scale on iron corroded in carbonated anoxic environments. *RSC Adv.* **7**, 20101–20115 (2017).
59. Saheb, M., Berger, P., Raimbault, L., Neff, D. & Dillmann, P. Investigation of iron long-term corrosion mechanisms in anoxic media using deuterium tracing. *J. Nucl. Mater.* **423**, 61–66 (2012).
60. Azoulay, I., Rémazeilles, C. & Refait, P. Determination of standard Gibbs free energy of formation of chukanovite and Pourbaix diagrams of iron in carbonated media. *Corros. Sci.* **58**, 229–236 (2012).
61. Saheb, M., Neff, D., Bellot-Gurlet, L. & Dillmann, P. Raman study of a deuterated iron hydroxycarbonate to assess long-term corrosion mechanisms in anoxic soils. *J. Raman Spectrosc.* **42**, 1100–1108 (2011).
62. Rajsiri, S., Kempshall, B., Schwarz, S. & Giannuzzi, L. FIB damage in silicon: amorphization or redeposition. *Microsc. Microanal.* **8**, 50–51 (2002).
63. Giannuzzi, L. A., Geurts, R. & Ringnalda, J. 2 keV Ga+ FIB milling for reducing amorphous damage in silicon. *Microsc. Microanal.* **11**, 828 (2005).
64. Michelin, A. et al. Investigation at the nanometre scale on the corrosion mechanisms of archaeological ferrous artefacts by STXM. *J. Anal. Spectrom.* **28**, 59–66 (2013).
65. Vernaz, E. Y. & Dussossoy, J. L. Current state of knowledge of nuclear waste glass corrosion mechanisms: the case of R7T7. *glass Appl. Geochem.* **7**, 13–22 (1992).
66. Gin, S. & Mestre, J. SON 68 nuclear glass alteration kinetics between pH 7 and pH 11.5. *J. Nucl. Mater.* **295**, 83–96 (2001).
67. Rebiscoul, D. et al. Morphological evolution of alteration layers formed during nuclear glass alteration: new evidence of a gel as a diffusive barrier. *J. Nucl. Mater.* **326**, 9–18 (2004).
68. Gin, S. et al. An international initiative on long-term behavior of high-level nuclear waste glass. *Mater. Today* **16**, 243–248 (2013).
69. Vienna, J. D., Ryan, J. V., Gin, S. & Inagaki, Y. Current understanding and remaining challenges in modeling long-term degradation of borosilicate nuclear waste glasses. *Int. J. Appl. Glas. Sci.* **4**, 283–294 (2013).
70. Gin, S. et al. Dynamics of self-reorganization explains passivation of silicate glasses. *Nat. Commun.* **9**, 2169 (2018).
71. Chevrier, V., Poulet, F. & Bibring, J.-P. Early geochemical environment of Mars as determined from thermodynamics of phyllosilicates. *Nature* **448**, 60 (2007).
72. Müller, G. & Förstner, U. Recent iron ore formation in Lake Malawi, Africa. *Miner. Depos.* **8**, 278–290 (1973).
73. Cole, T. G. The nature and origin of smectite in the Atlantis II Deep, Red Sea. *Can. Mineral.* **26**, 755–763 (1988).
74. Bischoff, J. L. A ferroan nontronite from the Red Sea geothermal system. *Clays Clay Miner.* **20**, 217–223 (1972).
75. Harder, H. Nontronite synthesis at low temperatures. *Chem. Geol.* **18**, 169–180 (1976).
76. Farmer, V. C., Krishnamurti, G. S. R. & HtJANG, P. M. Synthetic allophane and layer-silicate formation in SiO2-Al2O3-FeO-Fe2O3-MgO-H2O systems at 23 °C and 89 °C in a calcareous environment. *Clays Clay Miner.* **39**, 561–570 (1991).
77. Merola, R. B., Fournier, E. D. & McGuire, M. M. Spectroscopic investigations of Fe2 + complexation on nontronite clay. *Langmuir* **23**, 1223–1226 (2007).
78. Petit, S., Baron, F. & Decarreau, A. Synthesis of nontronite and other Fe-rich smectites: a critical review. *Clay Miner.* **52**, 469–483 (2017).
79. Lantenois, S. et al. Experimental study of smectite interaction with metal Fe at low temperature: 1. Smectite destabilization. *Clays Clay Miner.* **53**, 597–612 (2005).
80. Perronnet, M. et al. Evidence of a critical content in Fe (0) on FoCa7 bentonite reactivity at 80 °C. *Appl. Clay Sci.* **38**, 187–202 (2008).
81. Pignatelli, I. et al. A multi-technique characterization of cronstedtite synthesized by iron–clay interaction in a step-by-step cooling procedure. *Clays Clay Miner.* **61**, 277–289 (2013).
82. Pignatelli, I. et al. Iron–clay interactions: Detailed study of the mineralogical transformation of claystone with emphasis on the formation of iron-rich T–O phyllosilicates in a step-by-step cooling experiment from 90 °C to 40 °C. *Chem. Geol.* **387**, 1–11 (2014).
83. Wilson, J. C., Benbow, S., Sasamoto, H., Savage, D. & Watson, C. Thermodynamic and fully-coupled reactive transport models of a steel–bentonite interface. *Appl. Geochem.* **61**, 10–28 (2015).
84. Carrière, C. et al. New insights of Auger spectroscopy for the identification of Fe-Si compounds in iron/glass corrosion systems at nanoscale. *J. Electron Spectros. Relat. Phenom.* **235**, 51–59 (2019).
85. Aréna, H. et al. Impact of iron and magnesium on glass alteration: characterization of the secondary phases and determination of their solubility constants. *Appl. Geochem.* **82**, 119–133 (2017).
86. Thien, B. M. J., Godon, N., Ballestero, A., Gin, S. & Ayral, A. The dual effect of Mg on the long-term alteration rate of AVM nuclear waste glasses. *J. Nucl. Mater.* **427**, 297–310 (2012).
87. Christidis, G. E. M. J. Wilson (2013) rock-forming minerals, Vol. 3c, sheet silicates–clay minerals, 2nd edition. The Geological Society, London, 724 pp. £120. *Clay Miner.* **49**, 765–766 (2014).

88. Manceau, A., Chateigner, D. & Gates, W. P. Polarized EXAFS, distance-valence least-squares modeling (DVLS), and quantitative texture analysis approaches to the structural refinement of Garfield nontronite. *Phys. Chem. Miner.* **25**, 347–365 (1998).
89. Manceau, A. et al. Oxidation-reduction mechanism of iron in dioctahedral smectites: I. Crystal chemistry of oxidized reference nontronites. *Am. Mineral.* **85**, 133–152 (2000).
90. Schikorr, G. Über Eisen (II)-hydroxyd und ein ferromagnetisches Eisen (III)-hydroxyd. *Z. f.ür. Anorg. Allg. Chem.* **212**, 33–39 (1933).
91. Odziemkowski, M. S., Schuhmacher, T. T., Gillham, R. W. & Reardon, E. J. Mechanism of oxide film formation on iron in simulating groundwater solutions: Raman spectroscopic studies. *Corros. Sci.* **40**, 371–389 (1998).
92. Eggleton, R. A. Nontronite topotaxial after hedenbergite. *Am. Mineral.* **60**, 1063–1068 (1975).
93. Wang, Y., Jove-Colon, C. F. & Kuhlman, K. L. Nonlinear dynamics and instability of aqueous dissolution of silicate glasses and minerals. *Sci. Rep.* **6**, 30256 (2016).
94. Ribet, S. & Gin, S. Role of neoformed phases on the mechanisms controlling the resumption of SON68 glass alteration in alkaline media. *J. Nucl. Mater.* **324**, 152–164 (2004).
95. Aréna, H. et al. Impact of Zn, Mg, Ni and Co elements on glass alteration: additive effects. *J. Nucl. Mater.* **470**, 55–67 (2016).
96. Viviano, C. E., Moersch, J. E. & McSween, H. Y. Implications for early hydrothermal environments on Mars through the spectral evidence for carbonation and chloritization reactions in the Nili Fossae region. *J. Geophys. Res. Planets* **118**, 1858–1872 (2013).
97. Fernández-Caliani, J. C., Crespo, E., Rodas, M., Barrenechea, J. F. & Luque, F. J. Formation of nontronite from oxidative dissolution of pyrite disseminated in Precambrian felsic metavolcanics of the Southern Iberian Massif (Spain). *Clays Clay Miner.* **52**, 106–114 (2004).
98. Worden & Morad. Clay mineral cements in sandstones Richard H. Worden and Sadoon Morad. Special Publication Number 34 of the International Association of Sedimentologists, 2003; 489 pages. Clays Clay Miner. 52, 139–140 (2004).
99. De Echave, T., Tribet, M., Gin, S. & Jégou, C. Influence of iron on the alteration of the SON68 nuclear glass in the Callovo-Oxfordian groundwater. *Appl. Geochem.* **100**, 268–278 (2019).
100. Rebiscoul, D., Van Der Lee, A., Frugier, P., Ayral, A. & Gin, S. X-ray reflectometry characterization of SON 68 glass alteration films. *J. Non Cryst. Solids* **325**, 113–123 (2003).
101. Ribet & Godon. Altération par l'eau des verres borosilicatés Exemple des verres nucléaires. *Tech. l'ingénieur Matériaux résistance à la Corros. au Vieil*. (2014).
102. Advocat, T., Dussossoy, J.-L. & Petitjean, V. Vitrification des déchets radioactifs. *Tech. l'ingénieur Cycle du Combust. nucléaire Combust. usés déchets Radioact*. (2008).
103. Jollivet, P., Minet, Y., Nicolas, M. & Vernaz, É. Simulated alteration tests on non-radioactive SON 68 nuclear glass in the presence of corrosion products and environmental materials. *J. Nucl. Mater.* **281**, 231–243 (2000).
104. Delage, F. Etude de la fonction cinétique de dissolution d'un verre nucléaire, Université de Montpellier 2 (PhD thesis) (1992).
105. Fillet, S. Mécanismes de corrosion et comportement des actinides dans le verre nucléaire" R7T7", Université de Montpellier 2 (PhD thesis) (1987).
106. Francisco, P. C. M. et al. Interaction of FeII and Si under anoxic and reducing conditions: Structural characteristics of ferrous silicate co-precipitates. *Geochim. Cosmochim. Acta* **270**, 1–20 (2020).
107. Saldi, G. D. et al. Mineralogical evolution of Fe–Si-rich layers at the olivine-water interface during carbonation reactions. *Am. Mineral.* **100**, 2655–2669 (2015).
108. Daval, D. et al. Mechanism of wollastonite carbonation deduced from micro-to nanometer length scale observations. *Am. Mineral.* **94**, 1707–1726 (2009).
109. Holzlechner, G., Kubicek, M., Hutter, H. & Fleig, J. A novel ToF-SIMS operation mode for improved accuracy and lateral resolution of oxygen isotope measurements on oxides. *J. Anal. Spectrom.* **28**, 1080–1089 (2013).
110. Vanbellingen, Q. P. et al. Time-of-flight secondary ion mass spectrometry imaging of biological samples with delayed extraction for high mass and high spatial resolutions. *Rapid Commun. Mass Spectrom.* **29**, 1187–1195 (2015).
111. Cabaret, D., Sainctavit, P., Ildefonse, P. & Flank, A.-M. Full multiple scattering calculations of the X-ray absorption near edge structure at the magnesium K-edge in pyroxene. *Am. Mineral.* **83**, 300–304 (1998).
112. Cabaret, D. et al. Medium range structure of borosilicate glasses from Si K-edge XANES: a combined approach based on multiple scattering and molecular dynamics calculations. *J. Non Cryst. Solids* **289**, 1–8 (2001).
113. Fontaine, A. Spectroscopie d'absorption X (EXAFS et XANES) Application du rayonnement synchrotron. *Tech. l'ingénieur* (1989).
114. Levelut, C., Cabaret, D., Benoit, M., Jund, P. & Flank, A.-M. Multiple scattering calculations of the XANES Si K-edge in amorphous silica. *J. Non Cryst. Solids* **293**, 100–104 (2001).
115. Michelin, A. et al. Investigation at the nanometer scale on the corrosion mechanisms of the archaeological ferrous artifacts by STXM. *J. Anal. Spectrom.* **28**, 59–66 (2013).
116. Carrillo-Chavez, A. et al. Geochemistry and mineralogy of mine-waste material from a "skarn-type" deposit in central Mexico: modeling geochemical controls of metals in the surface environment. *J. Geochem. Explor.* **144**, 28–36 (2014).
117. Gailhanou, H. et al. Effects of a thermal perturbation on mineralogy and pore water composition in a clay-rock: an experimental and modeling study. *Geochim. Cosmochim. Acta* **197**, 193–214 (2017).
118. Calas, G., McMillan, P. F. & Bernier-Latmani, R. Environmental mineralogy: new challenges, new materials. *Elements* **11**, 247–252 (2015).
119. Bailey, L., Lekkerkerker, H. N. W. & Maitland, G. C. Smectite clay—inorganic nanoparticle mixed suspensions: phase behaviour and rheology. *Soft Matter* **11**, 222–236 (2015).

ACKNOWLEDGEMENTS

We thank the French National Centre for Scientific Research (CNRS), the French Alternative Energies and Atomic Energy Commission (CEA Saclay, CEA Marcoule) and the French National Radioactive Waste Management Agency (Andra) for the financial support of this work. The CIMAP laboratory is thankful to the French state managed by the National Research Agency through the "Investissements d'Avenir" program which reference is "ANR-11-EQPX-0020", by the Normandie Region and the "Fonds Européen de Développement Régional" FEDER. Part of the research described in this paper was performed at the Canadian Light Source, a national research facility of the University of Saskatchewan, which is supported by the Canada Foundation for Innovation (CFI), the Natural Sciences and Engineering Research Council (NSERC), the National Research Council (NRC), the Canadian Institutes of Health Research (CIHR), the Government of Saskatchewan, and the University of Saskatchewan.

AUTHOR CONTRIBUTIONS

C.C. wrote the paper, contributed to all experimental solid characterizations. P.D., D.N., and S.G. conceived the project and designed the experiment. L.G. and F.B. set up the experiment. E.G. and I.M. respectively machined the FIB foils and performed the TEM analyses in the GAL and in ICP. STXM analyses were conducted by E.F., J.D., C.C., P.D., and D.N. N.N. performed the ToF-SIMS analyses. M.S. and A.D. conducted the geochemical calculations. C.C., P.D., S.G., D.N., N.M., and C.M. interpreted the results. All the authors revised and approved the final paper.

COMPETING INTERESTS

The authors declare no competing interests.

ADDITIONAL INFORMATION

Supplementary information The online version contains supplementary material available at https://doi.org/10.1038/s41529-021-00160-x.

Correspondence and requests for materials should be addressed to C.C.

Reprints and permission information is available at http://www.nature.com/reprints

Publisher's note Springer Nature remains neutral with regard to jurisdictional claims in published maps and institutional affiliations.